Three-Dimensional Self-Assembly of Chalcopyrite Copper Indium Diselenide Nanocrystals into Oriented Films

Danielle C. Reifsnyder,[†] Xingchen Ye,[†] Thomas R. Gordon,[†] Chengyu Song,[§] and Christopher B. Murray*[,†,‡]

[†]Department of Chemistry and [‡]Department of Materials Science and Engineering, University of Pennsylvania, Philadelphia, Pennsylvania 19104, United States and [§]National Center for Electron Microscopy, Lawrence Berkeley National Laboratory, Berkeley, California 94720, United States

ABSTRACT $CuInSe_2$, which is one of the highest efficiency thin-film solar cell active layer materials, has been an attractive target for nanocrystal synthesis and manipulation. Here, we report unprecedented, simultaneous control of the synthesis and self-assembly behavior of $CuInSe_2$ nanocrystals. These nanocrystals are solution-processable, monodisperse tetragonal bipyramids that exhibit photoconductivity and self-assemble into crystallographically oriented thin films. Structural characterization indicates that these nanocrystals are tetragonal phase, as is used in high-efficiency, second-generation, thin-film solar cells. Elemental analysis indicates that approximately 1:1:2 Cu/In/Se stoichiometry can be achieved, and that the elemental composition can be adjusted from copper-rich to indium-rich with reaction time.

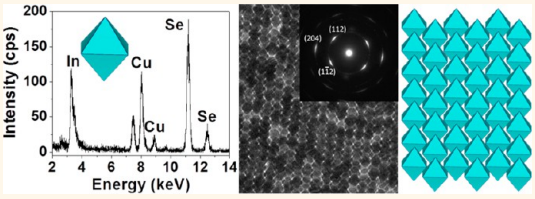

KEYWORDS: nanocrystal · copper indium diselenide · $CuInSe_2$ · I–III–VI · chalcopyrite · photovoltaics · photoconductivity

Copper indium diselenide ($CuInSe_2$) is one of the most promising materials for solar cell active layers.[1] Its band gap is ideally located within the solar spectrum (1.04 eV), and it has a high absorption coefficient on the order of 10^5 cm^{-1}.[2,3] Already, efficiencies of 20% have been achieved in thin-film devices based on $Cu(In_xGa_{1-x})Se_2$ (CIGS) materials.[4,5] State of the art methods for thin-film deposition require high temperature, vacuum conditions, and the overconsumption of expensive precursor materials due to inefficient deposition processes.[6] An approach to increasing the efficiency-to-cost ratio for solar cell production is the formation of active layer materials from arrays of solution-processable semiconducting nanocrystals synthesized from simple metal salts. To date, several reports have detailed the formation of active layers from chalcopyrite "nanocrystal inks", colloidal suspensions of nanocrystals with the desired phase composition but less than optimal control of the shape and size dispersion.[7−9] This report is intended to bridge the gap between what has been achieved with nanocrystal inks and the control of active layer composition and morphology that will be possible with uniform particles. Here, we report the synthesis of $CuInSe_2$ nanocrystals with dramatically improved uniformity and their integration into oriented films through self-assembly. With these materials, it will be feasible to direct the assembly of nanocrystals in active layer films. This work opens up the possibility for intentionally designed, nanoarchitectured active layer morphologies, which are composed of high-efficiency solar energy conversion materials.

A growing number of superstructures formed from colloidal nanocrystals have been reported in the literature. From the earliest reports of nanometer-sized colloid assembly (*e.g.*, iron oxide[10] and CdSe[11]) to multicomponent superlattices,[12] this has been a route toward controlling superstructure and film morphology and of patterning materials at nanometer length scales. In the case of inorganic nanocrystals, this phenomenon has given rise to a great diversity of structures, including crystalline[11,12] and quasicrystalline thin films,[13] aligned nanorod films formed with[14] and without[15] an electric field, and colloidal supercrystals.[11,16,17] The formation of these structures has been related to the uniformity of the nanocrystals,[10] the temperature of formation,[18] the molecular interactions between ligand molecules on nanocrystal surfaces, and the solvent–ligand

* Address correspondence to cbmurray@sas.upenn.edu.

Received for review February 17, 2013 and accepted May 2, 2013.

Published online May 02, 2013
10.1021/nn4008059

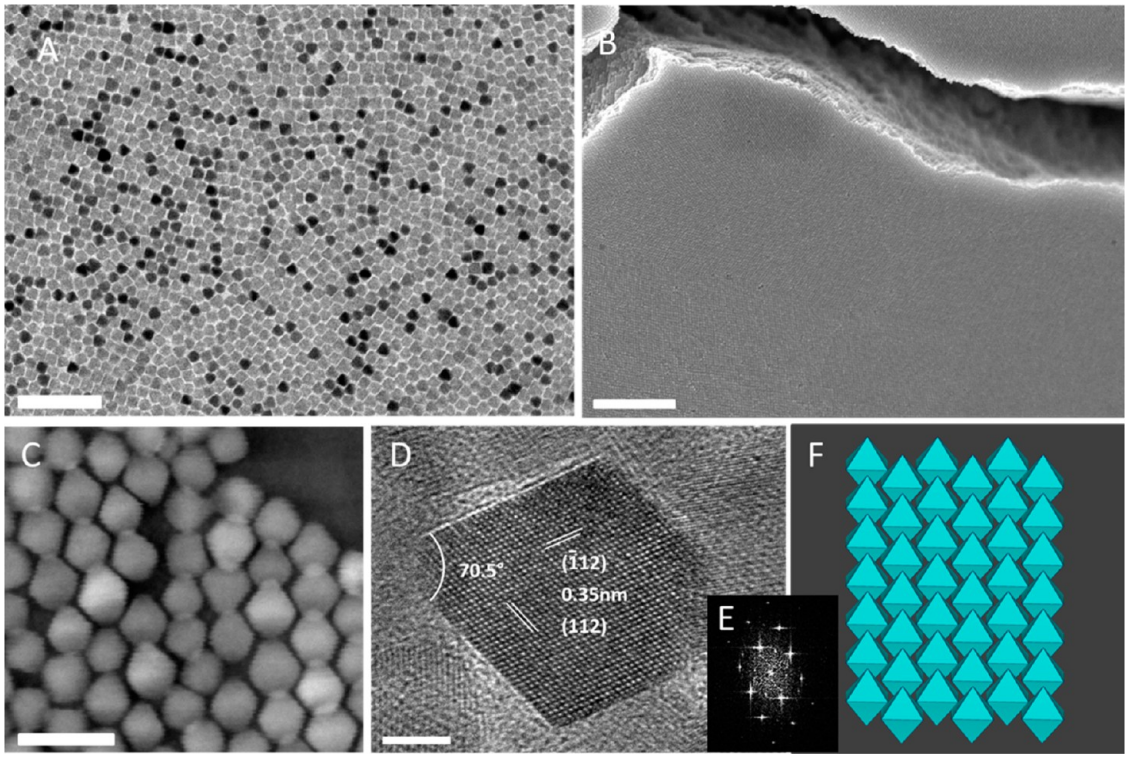

Figure 1. Electron microscopy of $CuInSe_2$ nanocrystals. (A) TEM image of a nanocrystal monolayer (scale bar 100 nm). (B) SEM image of an oriented $CuInSe_2$ nanocrystal film, displaying a thick, cracked region and a portion of the flat, ~100 μm^2 self-assembled area adjacent to it (scale bar 1 μm). (C) STEM image of a monolayer of oriented nanocrystals (scale bar 30 nm). (D) High-resolution TEM image of a single nanocrystal, displaying (112) lattice plane spacings (scale bar 5 nm). (E) FFT of nanocrystal shown in (D). (F) Model of self-assembled monolayer of $CuInSe_2$ nanocrystals as shown in B and C.

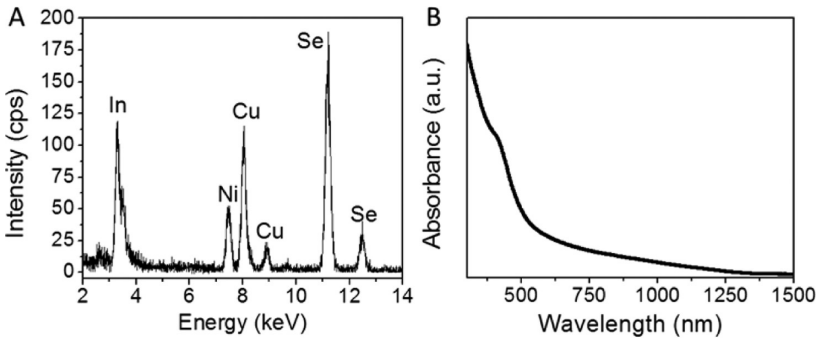

Figure 2. (A) EDS spectrum of approximately 500 $CuInSe_2$ nanocrystals (stoichiometry Cu/In/Se 25:21:54; Ni signal is from the Ni TEM grid used as a support) and (B) UV−visible absorption spectrum of $CuInSe_2$ nanocrystals.

interactions.[19] Forming films that are ordered creates an advantage because it makes systems easier to model and physically understand than disordered systems,[20] and more importantly, assembly of nanoscale building blocks has led to new, collective properties in thin films.[21,22] With building blocks of sufficient uniformity, new film geometries have become possible, including examples where self-assembled arrays and lithographic patterning are combined.[23]

So far, simultaneously controlling the shape, stoichiometry, and crystal structure of $CuInSe_2$ nanocrystals has proven difficult. In order to assemble nanocrystals into superlattices, they must be uniform enough to become the building blocks of a periodic superstructure. Recent progress in sulfide chalcopyrites is encouraging;[24−31] yet, despite a number of advances in compositional or structural control,[32−35] development of the selenium analogues, which have higher demonstrated efficiencies in conventional thin-film solar cells, has been less yielding. Recent successes in $CuInSe_2$ synthesis have produced various crystal phases formed as nanorings,[8] trigonal pyramids,[36] small (~3 nm) quantum-confined nanocrystals,[37] and hexagonal plates.[38] Here, we present a method to synthesize chalcopyrite phase $CuInSe_2$ nanocrystals that are derived from simple metal salt precursors and an air- and room-temperature-stable chalcogen source (selenium(IV) oxide). The successful application of selenium(IV) oxide

TABLE 1. Quantitative EDS Results of Several Batches of Cu–In–Se Nanocrystals

Result	Cu atomic %	In atomic %	Se atomic %	Reaction time
Very copper-rich	43	15	42	
Copper-rich	35	19	46	
Nearly-stoichiometric	25	21	54	Increasing
Nearly-stoichiometric	24	27	49	
Indium-rich	22	31	47	

to quantum dot synthesis, combined with its ease of handling, makes it an attractive precursor.[39,40] This work builds on the success of others in applying this approach to quaternary compounds of the I_2–II–IV–VI_4 family and opens up new opportunities to build nanoscale control into thin films for high-efficiency solar cell active layers.[41,42] As a result, we are able to produce nanocrystals that form extended, oriented, three-dimensional films. In order to produce films with the highest quality electronic and optical properties, strategies to control grain size and orientation must be established. Our monodisperse tetragonal bipyramids allow for formation of films with well-defined interparticle spacing, composition, grain size, and packing. In contrast to most thin-film deposition techniques, with our methods, it is also possible to gain control over crystal orientation at low temperature *via* solution processing.

RESULTS AND DISCUSSION

Electron Microscopy Characterization of $CuInSe_2$ Nanocrystal Shape and Structure. The synthesized $CuInSe_2$ nanocrystals (Figure 1D) are tetragonal bipyramids with dimensions of 16.5 nm × 23.4 nm. As shown in Figure 1A, the transmission electron microscopy (TEM) projection of a predominantly disordered monolayer indicates that, without ordering, the nanocrystals appear almost spherical with only slight visible faceting. The scanning electron microscopy (SEM) image of a large-area, self-assembled film in Figure 1B also does not elucidate the shape; however, when oriented nanocrystals are imaged by scanning TEM (STEM, Figure 1C), their bipyramidal shape becomes apparent (model shown in Figure 1F). In the high-resolution TEM (HRTEM) image (Figure 1D) and its fast Fourier transform (FFT, Figure 1E), this shape can also be observed in projection along the [20−1] zone axis.

Synthesis and Elemental Analysis of $CuInSe_2$ Nanocrystals. $CuInSe_2$ nanocrystal growth is accomplished by injecting the selenium source into a hot mixture of the copper and indium precursors. During growth, a copper-rich seed particle grows, and over time, indium incorporates into the structure, forming $CuInSe_2$ (Supporting Information Figure S1A,B and Figure 2A). This copper selenide quasi-seeded growth mechanism is similar to what has been observed in successful syntheses of uniform I_2–II–IV–VI_4 materials.[41,42] In the case of $CuInSe_2$, the product eventually becomes nearly stoichiometric, and with longer growth time, it becomes slightly indium-rich (Table 1). The nanocrystals shown in Figure 1 are nearly stoichiometric $CuInSe_2$ nanocrystals, as measured by energy-dispersive spectroscopy (EDS, Figure 2A). Their absorption is shown in Figure 2B.

Structural Characterization of $CuInSe_2$ Nanocrystals by X-ray Scattering. $CuInSe_2$ is known for its diversity of crystal structures.[43] In the bulk, it is mainly known for its tetragonal phase (α-CIS, space group $I\bar{4}2d$), which is analogous to the chalcopyrite phase of $CuFeS_2$ (from which this class of ternary materials, the chalcopyrite family, derives its name). This phase is based on the cubic zinc blende unit cell (derived from the diamond structure) but is tetragonal due to cation ordering in the *c*-direction. Its *c*-axis approximately equals twice the length of the *a*-axis, with slight tetragonal distortion. This distortion results from the unequal valence of Cu(I) and In(III) cations and the corresponding unequal lengths of Cu–Se and In–Se bonds, which are not isotropically distributed around the tetrahedral Se sites. Under some conditions (especially high-temperature growth), however, the Cu(I) and In(III) cations are disordered, resulting in the sphalerite structure (δ-CIS, space group $F\bar{4}2m$). When the cations are disordered, the structure reverts back to a face-centered cubic (fcc) unit cell.

Other indium-rich phases fall into the classifications of β-CIS and γ-CIS, which are largely derived from the diamond lattice, similarly to the sphalerite and chalcopyrite phases. Even in equilibrium structures, defects are very common. Due to its ternary nature, $CuInSe_2$ has a much greater accessible range of defect structures than related binary compounds.[44] In some cases, indium-rich phases have been uniquely identified, whereas some can also be considered as ordered defect/vacancy compounds (ODCs or OVCs) of the more common α-CIS phase.[45] A metastable tetragonal CuAu phase (space group $P\bar{4}m2$) has also been observed, primarily in coexistence with α-CIS since its energy of formation is very similar to that of α-CIS.[43] Under high pressure, a NaCl cubic structure has been reported in $CuInSe_2$ samples, appearing at 60 kbar when tested in a diamond-anvil cell.[46] In nanostructured materials, an additional hexagonal phase has been reported.[25,38,47] This cation-disordered phase is wurtzite, with a 50% probability that cation sites will be occupied by either Cu(I) and In(III).

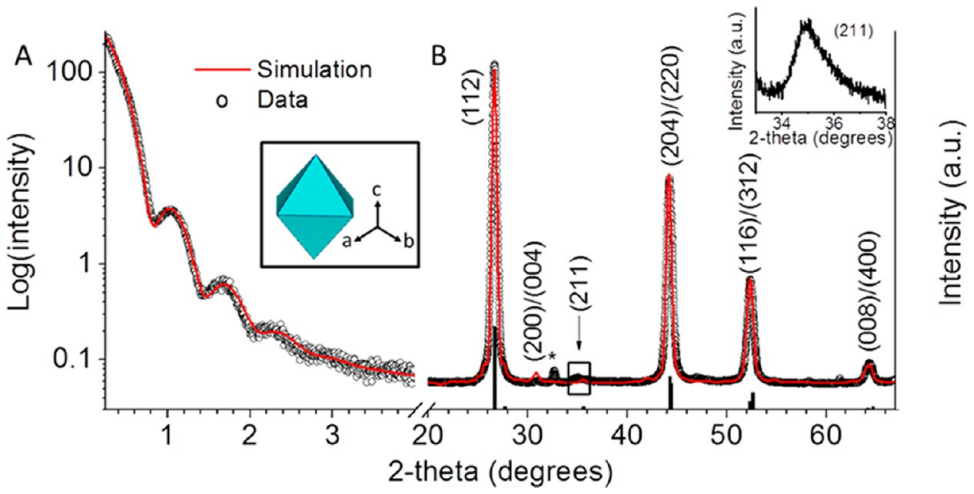

Figure 3. X-ray diffraction of $CuInSe_2$ nanocrystals. (A) Small-angle experimental pattern overlaid with simulation for $CuInSe_2$ tetragonal bipyramidal nanocrystals with a *c*-axis of 21.8 nm and a size dispersion of 8% (inset: nanocrystal model). (B) Experimental WAXS pattern overlaid with simulated wide-angle pattern (inset: experimentally observed characteristic chalcopyrite peak at 35°) with tetragonal $CuInSe_2$ JCPDS #01-081-1936 shown below.

Figure 3 shows X-ray diffraction (XRD) data for nearly stoichiometric $CuInSe_2$ nanocrystals. Figure 3A shows small-angle X-ray scattering (SAXS) from a dispersion of $CuInSe_2$ nanocrystals in a film of polyvinyl butyral resin (PVB), along with the SAXS pattern simulated for a sample with the dimensions $a = 15.4$ nm and $c = 21.8$ nm and a size dispersion of 8%. The SAXS ringing pattern and the high quality of the fit confirm that the sample is as uniform at the bulk level as it appears over selected areas by electron microscopy. Figure 3B shows the experimental and simulated wide-angle X-ray scattering (WAXS) patterns. The data match the standard $CuInSe_2$ pattern (JCPDS #01-081-1936) well, and the intensities of the observed peaks correspond to the intensities fit with a tetragonal bipyramidal model (*c*-axis = 21.8 nm), supporting our observations of the morphology.

Since the $CuInSe_2$ tetragonal and sphalerite patterns are almost identical, in order to differentiate between them, it is important to observe a unique chalcopyrite peak.[8] The low-intensity, characteristic chalcopyrite (211) peak is visible in both the experimental data and the simulation (inset: (211) peak). This peak clearly exists in the as-synthesized nanocrystal sample and proves the existence of the chalcopyrite, cation-ordered structure. Partial coexistence of the sphalerite and CuAu phases cannot be ruled out, however, since the XRD signatures of these structures are very similar.[43] A low-intensity peak at 32.7° is marked with an asterisk, which matches the NaCl $CuInSe_2$ phase but could also arise from a small amount of CuSe.

While most of the above-mentioned phases are fundamentally stoichiometric 1:1:2, a variety of indium-rich ordered defect compounds based on the tetragonal structure are stable in the bulk and often occur.[48] Several observed stoichiometries are 1:3:5, 1:5:8, 2:4:7, and 3:5:9. Some of these structures likely result from reduced formation energies of cation vacancy sites in chalcopyrites and others as the result of energetically stabilized defect pairs. However, all of these ordered defect structures are significantly indium-rich, which we do not observe here. Our samples are nearly stoichiometric, slightly indium-rich, or copper-rich. This could be due to nanoscale stabilization of copper-rich structures, but it could also be a direct result of the synthetic pathway, in which a predominantly copper selenide-rich seed particle is formed, which gradually incorporates indium as the reaction proceeds (Supporting Information Figure S1A,B and Figure 2A). Indium-rich phases are also often difficult to distinguish by XRD, so elemental analysis must be employed to aid in differentiation. For the experimental XRD pattern shown (Figure 2A), however, elemental analysis indicates near stoichiometry.

Photoconductive Response of $CuInSe_2$ Nanocrystal Thin Films. As potential solar cell active layer materials, it is important that the $CuInSe_2$ nanocrystals reported here can be incorporated into thin films that exhibit photoconductivity.[49,35] Therefore, we demonstrate that a spin-casted, ligand-exchanged film of $CuInSe_2$ nanocrystals shows dark conductivity under applied bias and enhanced photocurrent under incident 30 mW/cm^2 488 nm radiation. Films were spin-casted onto (3-mercaptopropyl)trimethoxysilane-treated quartz substrates with prepatterned gold electrodes.[50] These films were alternately spin-casted from chloroform and soaked in an ammonium thiocyanate solution in acetone to achieve ligand exchange.[51] Figure 4 shows the device geometry used (Figure 4A), an SEM image of a ligand-exchanged film, which indicates that the nanocrystals are still distinct and undistorted after treatment (Figure 4B), and the photoconductive response of the ligand-exchanged $CuInSe_2$ film

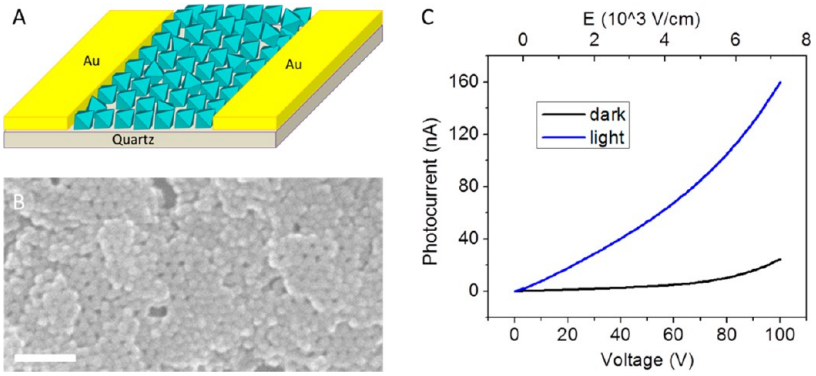

Figure 4. Photoconductivity of $CuInSe_2$ nanocrystal films. (A) Device geometry used to measure photoconductivity, (B) SEM image of a ligand-exchanged film (scale bar 100 nm), and (C) *I*−*V* curves of a $CuInSe_2$ film, in the dark (black) and under 30 mW/cm^2 488 nm excitation (blue).

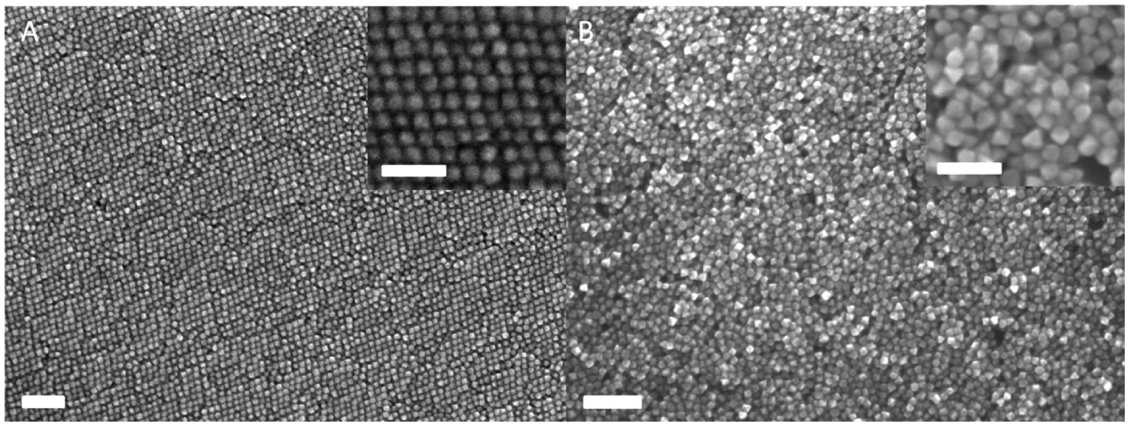

Figure 5. Scanning electron microscopy (SEM) images (scale bars 100 nm) and high-resolution SEM images (insets, scale bars 50 nm) of (A) ordered $CuInSe_2$ nanocrystal film and (B) disordered $CuInSe_2$ nanocrystal film.

(Figure 4C). Across the 150 μm channel measured, the photocurrent showed a 10−15-fold increase over the dark current for most of the voltage range studied, depending on the applied bias. For example, at 20 V, the current increased from 1.2 to 18 nA (15-fold increase), and at 80 V, the current increased from 10.5 nA in the dark to 105 nA (10-fold increase) under illumination. With optimization of film deposition and treatment conditions, it should be possible to further improve the photoconductive response of these $CuInSe_2$ nanocrystal films.

Self-Assembly of $CuInSe_2$ Nanocrystals into Oriented, Single-Crystalline, Multilayer Structures. When nanocrystals are able to self-assemble, an avenue is opened for construction of films, which can be structurally modulated at the nanoscale. Self-assembled structures form when particle size and shape are uniform enough that nanocrystals can become the individual building blocks in a regular, often periodic, structure. Many examples of nanocrystal assembly have been observed, but this area is largely unexplored in the case of $CuInSe_2$ nanocrystals. Occasionally, $CuInSe_2$ samples have been reported to form regularly packed monolayers, but never ordered, multilayer structures.[36,38] Here, we present results of nearly stoichiometric nanocrystals that form large, multi-micrometer-sized domains of oriented nanocrystals (Figure 5). Forming large-area, close-packed structures of $CuInSe_2$ has important implications for the construction of solar cell active layers since it not only assures dense packing and close contact between edges of neighboring nanocrystals for charge transport but also allows for structural and electronic modulation to be built into the film.

Figure 6 shows TEM and SEM images and a selected-area wide-angle electron diffraction (SAWED) pattern of three-dimensional arrays of ordered $CuInSe_2$ nanocrystals. The end-to-end packing motif shown is similar to that of In_2O_3[52] and Pt[53] octahedra, as well as $CoFe_2O_4$ truncated octahedra.[54] When $CuInSe_2$ nanocrystals self-assemble, their anisotropic, faceted nature creates a structure that takes on single-crystalline behavior (Figure 6A). The electron diffraction pattern in Figure 6A shows almost complete transition to single-crystalline-like packing. While this phenomenon has been observed in phosphorescent nanocrystals,[55] it is particularly interesting for semiconducting nanocrystals because crystal anisotropy and orientation have an effect on the directionality of energy levels and therefore have implications for charge transport.

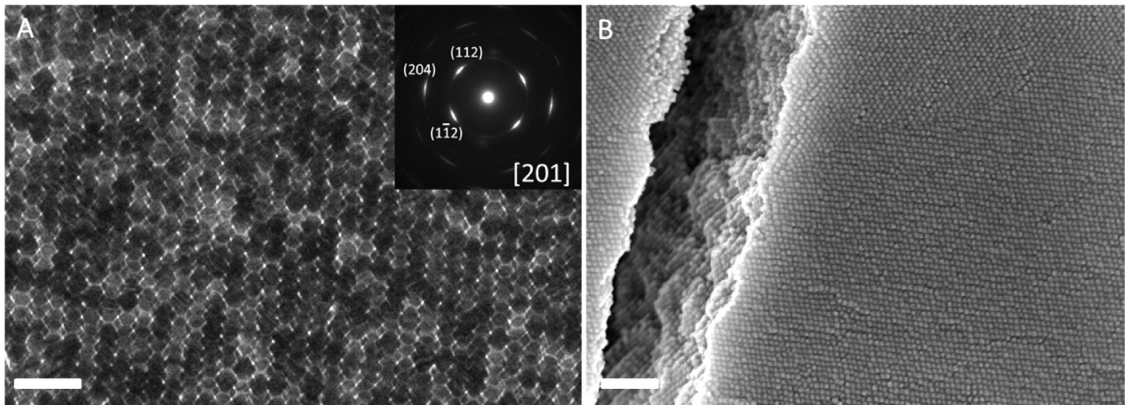

Figure 6. Electron microscopy of self-assembled, oriented films of $CuInSe_2$ nanocrystals. (A) TEM image of self-assembled $CuInSe_2$ nanocrystals with SAWED inset showing a diffraction pattern like that along the [20−1] zone axis of a single-crystal bulk, tetragonal sample (scale bar 50 nm) and (B) high-magnification SEM image of a cracked, oriented film, showing the smooth film surface and uninterrupted ordering of nanocrystals through the thickness of the film (scale bar 150 nm).

Figure 6A shows a single-domain superlattice, the electron diffraction of which produces a spot pattern like that along the [20−1] zone axis of a single-crystal, bulk tetragonal sample. The SEM image in Figure 6B shows that the film is both smooth across its surface and ordered throughout its depth.

CONCLUSIONS

In summary, we have presented a method to make oriented films of self-assembled $CuInSe_2$ nanocrystals. This provides a way to control composition and film morphology that should lead to the ability to make efficient solar cell active layers from $CuInSe_2$ nanocrystals. We simultaneously control the structural uniformity, crystal phase, and composition of $CuInSe_2$ nanocrystals and demonstrate that these nanocrystals are photoconductive and able to self-assemble into three-dimensional, oriented films. With these building blocks, it should be possible not only to deposit high-quality $CuInSe_2$ films but also to build structural complexity into ordered, multicomponent films. This work should open up new avenues to increase the efficiency of photovoltaic devices by deliberately patterning high-efficiency photovoltaic materials at the nanoscale.

EXPERIMENTAL SECTION

Chemicals. All chemicals were used as received: selenium(IV) oxide (SeO_2, Acros, 99.8%), 1-octadecene (ODE, Aldrich, 90% technical grade), hexadecylamine (HDA, Aldrich, 90%), *n*-octadecylphosphonic acid (ODPA, PCI Synthesis, ≥99%), oleic acid (OlAc, Aldrich, 90% technical grade), copper(I) chloride (CuCl, Sigma-Aldrich, >99%), indium(III) chloride ($InCl_3$, Aldrich, 99.999%), Butvar-B98 (PVB (polyvinyl butyral resin), Sigma), chloroform ($CHCl_3$, Fisher Scientific, ACS reagent grade), isopropyl alcohol (IPA, Fisher Scientific, ACS reagent grade), tetrachloroethylene (TCE, Sigma-Aldrich, ≥99%), toluene (Fisher Scientific, ACS reagent grade), and ethanol (Decon Laboratories, 190 proof). For work under nitrogen atmosphere, solvents were dried on an alumina column or over calcium hydride (Acros Organics, *ca.* 93%, extra pure, 0−2 mm grain size).

Nanocrystal Synthesis. All precursor preparation and synthesis was carried out on a Schlenk line under nitrogen environment. First, a 0.8 M stock solution of SeO_2 in ODE was prepared by adding 1.775 g (16 mmol) of SeO_2 to 20 mL of ODE. While stirring under nitrogen atmosphere, this mixture was heated to 180 °C overnight (~12 h). This Se−ODE solution was then cooled to 120 °C prior to injection, which kept it homogeneous and unsolidified. Separately, 0.050 g of CuCl (0.5 mmol), 0.111 g of $InCl_3$ (0.5 mmol), 1.230 g of HDA (5 mmol), 0.066 g of ODPA (0.2 mmol), and 10 mL of ODE were loaded into a 50 mL three-neck flask. Before use, $InCl_3$ was stored under nitrogen to prevent water adsorption. This reaction flask was heated to 200 °C for 1 h under nitrogen atmosphere and then subsequently heated to 290 °C. At 290 °C, 4 mL of the 120 °C Se−ODE solution was rapidly injected into the reaction flask containing the metal precursors. Upon injection, the temperature fell as low as 250 °C but recovered to 285−290 °C. At 10−12 min after injection, the heating mantle was removed to allow the reaction mixture to cool to room temperature. As the reaction cooled, 5 mL of room-temperature OlAc was injected at 200 °C. For the reaction vessel, a glass-coated, type K thermocouple was used to avoid reaction of the precursors with the metal thermocouple surface. All temperatures were calibrated by heating a flask of ODE that simultaneously contained both a glass-coated and an uncoated thermocouple.

Isolation of Nanocrystals. The contents of the reaction flask were transferred into a 50 mL centrifuge tube, to which 10 mL of $CHCl_3$ was added. This mixture was sonicated in a warm water bath for 5 min and centrifuged at 4000 rpm for 5 min to precipitate nanocrystalline products. The light brown supernatant was discarded, and the dark brown precipitate was redispersed in 20 mL of $CHCl_3$. This suspension was sonicated in a warm water bath for 5 min and centrifuged for 1 min at 2000 rpm to precipitate any insoluble, bulk-like side products. The precipitate was discarded, and 10 mL of IPA was added to the supernatant. The IPA mixture was centrifuged at 4000 rpm for 3 min to precipitate the nanocrystals. The final precipitate was then redispersed in 20 mL of $CHCl_3$, sonicated in a warm water bath for 5 min, and filtered through a 0.2 μm PTFE filter. Nanocrystals used for photoconductivity measurements were centrifuged in the glovebox under nitrogen. This required addition of $CHCl_3$ directly to the reaction flask, upon cooling to 70 °C, and a cannula transfer to a nitrogen-filled flask that could be introduced into the glovebox.

Preparation of Nanocrystal Films. Disordered films and monolayers were prepared by placing a drop of $CHCl_3$ solution onto a carbon-coated copper or nickel transmission electron microscopy (TEM) grid. Allowing a drop to slowly collapse onto the

grid resulted in domains of multilayer self-assembly at higher concentrations. Larger self-assembled films were prepared by precipitating the nanocrystals from $CHCl_3$ and redispersing them in TCE for slow evaporation. Best results were obtained when a portion of freshly prepared solution was precipitated with IPA and directly redispersed in TCE for deposition. A TEM grid was placed on the bottom of a 20 mL vial into which 40 μL of $CuInSe_2$ solution was added. This vial was tilted by 45° from the vertical, placed in a vacuum oven set at 60 °C, and left under vacuum overnight. Films for photoconductivity measurements were deposited under nitrogen atmosphere by spin-casting from $CHCl_3$ onto prepatterned, pretreated photoconductivity substrates. For photoconductivity substrate preparation, gold electrodes (channel length 150 μm, channel width 2.25 mm) were thermally evaporated onto a quartz substrate, and then the substrate was soaked in a 5% v/v solution of (3-mercaptopropyl)trimethoxysilane in toluene at 40 °C for 4 h.[50] It was then rinsed successively in toluene, a 1:1 toluene/ethanol mixture and ethanol. $CuInSe_2$ films were spin-casted from $CHCl_3$ at 2500 rpm for 30 s and then soaked successively in an ammonium thiocyanate in acetone solution (0.1 g/10 mL) for 1 min and two acetone rinses for 30 s each.[51] Nanocrystal deposition and treatment was repeated up to 15 times. After film deposition, the electrodes were isolated and a glass coverslip was epoxied over the channels, encapsulating them in nitrogen atmosphere.

Characterization. Nanocrystals were drop-cast from $CHCl_3$ onto 300 mesh carbon-coated copper and 200 mesh carbon-coated nickel transmission electron microscopy (TEM) grids for analysis. The copper grids were used for larger-area imaging, performed on a JEOL JEM1400 TEM with a LaB_6 filament, operating at 120 kV and equipped with an SC1000 ORIUS CCD camera. Selected-area wide-angle electron diffraction (SAWED) was performed using a camera length of 25 cm and also on a JEOL JEM1400 TEM. The nickel grids were used for high-resolution TEM (HRTEM) imaging, scanning TEM (STEM) imaging, and energy-dispersive spectroscopy (EDS) for elemental analysis, which were performed on a Philips CM300FEG/UT TEM with a field emission gun (FEG) and low spherical aberration (C_s = 0.60 mm), operating at 300 kV; on a CM200/FEG TEM/STEM, operating at 200 kV; and on a JEOL 2010F TEM/STEM, equipped with a FEG, operating at 200 kV. EDS quantitative elemental analysis was performed using Bruker Espirit software on the 2010F and Oxford Inca software on the CM200. Wide-angle X-ray scattering (WAXS) was performed on a Rigaku Smartlab diffractometer equipped with a 2.2 kW sealed tube generator, using a Cu Kα (λ = 1.54056 Å) source. For WAXS, nanocrystal solutions in $CHCl_3$ were concentrated several times and drop-casted onto Si(100) wafers, gently tilting the substrate back and forth while drying to ensure formation of disordered films for analysis and modeling. WAXS nanocrystal modeling was performed using the discretized form of the Debye equation with atomic form factors derived from Cromer-Mann coefficients.[56] Small-angle X-ray scattering (SAXS) was performed on a multiangle X-ray diffractometer system equipped with a Bruker Nonius FR591 rotating-anode X-ray generator, Osmic Max-Flux optics with pinhole collimation, and a Bruker Hi-Star multiwire detector. Samples for SAXS were prepared by mixing 10% w/v PVB in chloroform, mixing with nanocrystals dispersed in chloroform, and spreading on a glass slide to dry. SAXS samples were dried under ambient conditions for approximately 1 h and then at 40 °C for 2 h, after which time, they were peeled off of the glass slide as a flexible film. Photocurrent measurements were performed by illuminating samples with the 488 nm line of an Innova 70C Spectrum Ar:Kr laser. The intensity at the sample was 30 mW/cm^2, and the beam diameter was 3.1 mm. Photo- and dark current were recorded by a digital electrometer (Keithley 6517b). The voltage was scanned in 1 V increments from 0 to 100 V.

Conflict of Interest: The authors declare no competing financial interest.

Acknowledgment. We thank Dr. Douglas M. Yates at the Penn Regional Nanotechnology Facility for TEM training and assistance, Dr. Paul A. Heiney for SAXS training and assistance, Soong Ju Oh and E.D. Goodwin for photocurrent measurement training, and Jun Chen for helpful discussions. D.C.R. and C.B.M. acknowledge support from the U.S. Department of Energy Office of Basic Energy Sciences, Division of Materials Science and Engineering (Award No. DE-SC0002158). D.C.R. acknowledges additional support from the NSF-IGERT program (Grant DGE-0221664). C.B.M. is also grateful to the Richard Perry University Professorship. X.Y. acknowledges support from the Office of Naval Research (ONR) Multidisciplinary University Research Initiative (MURI) on Optical Metamaterials (Award No. N00014-10-1-0942). T.R.G. acknowledges support from the National Science Foundation through the Nano/Bio Interface Center at the University of Pennsylvania (Grant DMR08-32802). This work was performed in part at NCEM, which is supported by the Office of Science, Office of Basic Energy Sciences of the U.S. Department of Energy under Contract No. DE-AC02-05CH11231.

Supporting Information Available: Additional figures and elemental characterization. This material is available free of charge *via* the Internet at http://pubs.acs.org.

REFERENCES AND NOTES

1. Tiwari, A. N.; Lincot, D.; Contreras, M. The Time for CIGS. *Prog. Photovoltaics* **2010**, *18*, 389–389.
2. Shay, J. L.; Tell, B.; Kasper, H. M.; Schiavone, L. M. Electronic Structure of $AgInSe_2$ and $CuInSe_2$. *Phys. Rev. B* **1973**, *7*, 4485–4490.
3. Rockett, A.; Birkmire, R. W. $CuInSe_2$ for Photovoltaic Applications. *J. Appl. Phys.* **1991**, *70*, R81–R97.
4. Repins, I.; Contreras, M. A.; Egaas, B.; DeHart, C.; Scharf, J.; Perkins, C. L.; To, B.; Noufi, R. 19.9%-Efficient ZnO/CdS/$CuInGaSe_2$ Solar Cell with 81.2% Fill Factor. *Prog. Photovoltaics* **2008**, *16*, 235–239.
5. Jackson, P.; Hariskos, D.; Lotter, E.; Paetel, S.; Wuerz, R.; Menner, R.; Wischmann, W.; Powalla, M. New World Record Efficiency for Cu(In,Ga)Se_2 Thin-Film Solar Cells Beyond 20%. *Prog. Photovoltaics* **2011**, *19*, 894–897.
6. Hibberd, C. J.; Chassaing, E.; Liu, W.; Mitzi, D. B.; Lincot, D.; Tiwari, A. N. Non-vacuum Methods for Formation of Cu(In,Ga)$(Se,S)_2$ Thin Film Photovoltaic Absorbers. *Prog. Photovoltaics* **2010**, *18*, 434–452.
7. Panthani, M. G.; Akhavan, V.; Goodfellow, B.; Schmidtke, J. P.; Dunn, L.; Dodabalapur, A.; Barbara, P. F.; Korgel, B. A. Synthesis of $CuInS_2$, $CuInSe_2$, and Cu$(In_xGa_{1-x})Se_2$ (CIGS) Nanocrystal "Inks" for Printable Photovoltaics. *J. Am. Chem. Soc.* **2008**, *130*, 16770–16777.
8. Guo, Q.; Kim, S. J.; Kar, M.; Shafarman, W. N.; Birkmire, R. W.; Stach, E. A.; Agrawal, R.; Hillhouse, H. W. Development of $CuInSe_2$ Nanocrystal and Nanoring Inks for Low-Cost Solar Cells. *Nano Lett.* **2008**, *8*, 2982–2987.
9. Guo, Q.; Ford, G. M.; Hillhouse, H. W.; Agrawal, R. Sulfide Nanocrystal Inks for Dense Cu$(In_{1-x}Ga_x)(S_{1-y}Se_y)_2$ Absorber Films and Their Photovoltaic Performance. *Nano Lett.* **2009**, *9*, 3060–3065.
10. Bentzon, M. D.; van Wonterghem, J.; Mørup, S.; Thölén, A.; Koch, C. J. W. Ordered Aggregates of Ultrafine Iron Oxide Particles: `Super Crystals'. *Philos. Mag. B* **1989**, *60*, 169–178.
11. Murray, C. B.; Kagan, C. R.; Bawendi, M. G. Self-Organization of CdSe Nanocrystallites into Three-Dimensional Quantum Dot Superlattices. *Science* **1995**, *270*, 1335–1338.
12. Shevchenko, E. V.; Talapin, D. V.; Kotov, N. A.; O'Brien, S.; Murray, C. B. Structural Diversity in Binary Nanoparticle Superlattices. *Nature* **2006**, *439*, 55–59.
13. Talapin, D. V.; Shevchenko, E. V.; Bodnarchuk, M. I.; Ye, X.; Chen, J.; Murray, C. B. Quasicrystalline Order in Self-Assembled Binary Nanoparticle Superlattices. *Nature* **2009**, *461*, 964–967.
14. Ryan, K. M.; Mastroianni, A.; Stancil, K. A.; Liu, H.; Alivisatos, A. P. Electric-Field-Assisted Assembly of Perpendicularly Oriented Nanorod Superlattices. *Nano Lett.* **2006**, *6*, 1479–1482.
15. Baker, J. L.; Widmer-Cooper, A.; Toney, M. F.; Geissler, P. L.; Alivisatos, A. P. Device-Scale Perpendicular Alignment of Colloidal Nanorods. *Nano Lett.* **2010**, *10*, 195–201.

16. Wang, T.; Wang, X.; LaMontagne, D.; Wang, Z.; Wang, Z.; Cao, Y. C. Shape-Controlled Synthesis of Colloidal Superparticles from Nanocubes. *J. Am. Chem. Soc.* **2012**, *134*, 18225–18228.
17. Wang, T.; Zhuang, J.; Lynch, J.; Chen, O.; Wang, Z.; Wang, X.; LaMontagne, D.; Wu, H.; Wang, Z.; Cao, Y. C. Self-Assembled Colloidal Nanorods. *Science* **2012**, *338*, 358–363.
18. Bodnarchuk, M. I.; Kovalenko, M. V.; Heiss, W.; Talapin, D. V. Energetic and Entropic Contributions to Self-Assembly of Binary Nanocrystal Superlattices: Temperature as the Structure-Directing Factor. *J. Am. Chem. Soc.* **2010**, *132*, 11967–11977.
19. Bian, K.; Choi, J. J.; Kaushik, A.; Clancy, P.; Smilgies, D.-M.; Hanrath, T. Shape-Anisotropy Driven Symmetry Transformations in Nanocrystal Superlattice Polymorphs. *ACS Nano* **2011**, *5*, 2815–2823.
20. Remacle, F.; Collier, C. P.; Markovich, G.; Heath, J. R.; Banin, U.; Levine, R. D. Networks of Quantum Nanodots: The Role of Disorder in Modifying Electronic and Optical Properties. *J. Phys. Chem. B* **1998**, *102*, 7727–7734.
21. Urban, J. J.; Talapin, D. V.; Shevchenko, E. V.; Kagan, C. R.; Murray, C. B. Synergism in Binary Nanocrystal Superlattices Leads to Enhanced p-Type Conductivity in Self-Assembled PbTe/Ag_2Te Thin Films. *Nat. Mater.* **2007**, *6*, 115–121.
22. Dong, A.; Chen, J.; Vora, P. M.; Kikkawa, J. M.; Murray, C. B. Binary Nanocrystal Superlattice Membranes Self-Assembled at the Liquid−Air Interface. *Nature* **2010**, *466*, 474–477.
23. Akey, A.; Lu, C.; Yang, L.; Herman, I. P. Formation of Thick, Large-Area Nanoparticle Superlattices in Lithographically Defined Geometries. *Nano Lett.* **2010**, *10*, 1517–1521.
24. Uehara, M.; Watanabe, K.; Tajiri, Y.; Nakamura, H.; Maeda, H. Synthesis of $CuInS_2$ Fluorescent Nanocrystals and Enhancement of Fluorescence by Controlling Crystal Defect. *J. Chem. Phys.* **2008**, *129*, 134709.
25. Pan, D.; An, L.; Sun, Z.; Hou, W.; Yang, Y.; Yang, Z.; Lu, Y. Synthesis of Cu−In−S Ternary Nanocrystals with Tunable Structure and Composition. *J. Am. Chem. Soc.* **2008**, *130*, 5620–5621.
26. Li, L.; Daou, T. J.; Texier, I.; Chi, T. T. K.; Liem, N. Q.; Reiss, P. Highly Luminescent $CuInS_2$/ZnS Core/Shell Nanocrystals: Cadmium-Free Quantum Dots for *In Vivo* Imaging. *Chem. Mater.* **2009**, *21*, 2422–2429.
27. Xie, R.; Rutherford, M.; Peng, X. Formation of High-Quality I-III-VI Semiconductor Nanocrystals by Tuning Relative Reactivity of Cationic Precursors. *J. Am. Chem. Soc.* **2009**, *131*, 5691–5697.
28. Kruszynska, M.; Borchert, H.; Parisi, J.; Kolny-Olesiak, J. Synthesis and Shape Control of $CuInS_2$ Nanoparticles. *J. Am. Chem. Soc.* **2010**, *132*, 15976–15986.
29. Zhong, H.; Lo, S. S.; Mirkovic, T.; Li, Y.; Ding, Y.; Li, Y.; Scholes, G. D. Noninjection Gram-Scale Synthesis of Monodisperse Pyramidal $CuInS_2$ Nanocrystals and Their Size-Dependent Properties. *ACS Nano* **2010**, *4*, 5253–5262.
30. Li, L.; Pandey, A.; Werder, D. J.; Khanal, B. P.; Pietryga, J. M.; Klimov, V. I. Efficient Synthesis of Highly Luminescent Copper Indium Sulfide-Based Core/Shell Nanocrystals with Surprisingly Long-Lived Emission. *J. Am. Chem. Soc.* **2011**, *133*, 1176–1179.
31. Singh, A.; Coughlan, C.; Laffir, F.; Ryan, K. M. Assembly of $CuIn_{1-x}Ga_xS_2$ Nanorods into Highly Ordered 2D and 3D Superstructures. *ACS Nano* **2012**, *6*, 6977–6983.
32. Castro, S. L.; Bailey, S. G.; Raffaelle, R. P.; Banger, K. K.; Hepp, A. F. Nanocrystalline Chalcopyrite Materials ($CuInS_2$ and $CuInSe_2$) *via* Low-Temperature Pyrolysis of Molecular Single-Source Precursors. *Chem. Mater.* **2003**, *15*, 3142–3147.
33. Zhong, H.; Li, Y.; Ye, M.; Zhu, Z.; Zhou, Y.; Yang, C.; Li, Y. A Facile Route To Synthesize Chalcopyrite $CuInSe_2$ Nanocrystals in Non-coordinating Solvent. *Nanotechnology* **2007**, *18*, 025602.
34. Allen, P. M.; Bawendi, M. G. Ternary I-III-VI Quantum Dots Luminescent in the Red to Near-Infrared. *J. Am. Chem. Soc.* **2008**, *130*, 9240–9241.
35. Tang, J.; Hinds, S.; Kelley, S. O.; Sargent, E. H. Synthesis of Colloidal $CuGaSe_2$, $CuInSe_2$, and Cu(InGa)Se_2 Nanoparticles. *Chem. Mater.* **2008**, *20*, 6906–6910.
36. Koo, B.; Patel, R. N.; Korgel, B. A. Synthesis of $CuInSe_2$ Nanocrystals with Trigonal Pyramidal Shape. *J. Am. Chem. Soc.* **2009**, *131*, 3134–3135.
37. Zhong, H.; Wang, Z.; Bovero, E.; Lu, Z.; van Veggel, F. C. J. M.; Scholes, G. D. Colloidal $CuInSe_2$ Nanocrystals in the Quantum Confinement Regime: Synthesis, Optical Properties, and Electroluminescence. *J. Phys. Chem. C* **2011**, *115*, 12396–12402.
38. Wang, J.-J.; Wang, Y.-Q.; Cao, F.-F.; Guo, Y.-G.; Wan, L.-J. Synthesis of Monodispersed Wurtzite Structure $CuInSe_2$ Nanocrystals and Their Application in High-Performance Organic-Inorganic Hybrid Photodetectors. *J. Am. Chem. Soc.* **2010**, *132*, 12218–12221.
39. Chen, O.; Chen, X.; Yang, Y.; Lynch, J.; Wu, H.; Zhuang, J.; Cao, Y. C. Synthesis of Metal-Selenide Nanocrystals Using Selenium Dioxide as the Selenium Precursor. *Angew. Chem., Int. Ed.* **2008**, *47*, 8638–8641.
40. Garcia-Rodriguez, R.; Hendricks, M. P.; Cossairt, B.; Liu, H.; Owen, J. S. Conversion Reactions of Cadmium Chalcogenide Nanocrystal Precursors. *Chem. Mater.* **2013**, *25*, 1233–1249.
41. Ibáñez, M.; Cadavid, D.; Zamani, R.; García-Castelló, N.; Izquierdo-Roca, V.; Li, W.; Fairbrother, A.; Prades, J. D.; Shavel, A.; Arbiol, J.; *et al.* Composition Control and Thermoelectric Properties of Quaternary Chalcogenide Nanocrystals: The Case of Stannite $Cu_2CdSnSe_4$. *Chem. Mater.* **2012**, *24*, 562–570.
42. Ibáñez, M.; Zamani, R.; Li, W.; Shavel, A.; Arbiol, J.; Morante, J. R.; Cabot, A. Extending the Nanocrystal Synthesis Control to Quaternary Compositions. *Cryst. Growth Des.* **2012**, *12*, 1085–1090.
43. Stanbery, B. J. Copper Indium Selenides and Related Materials for Photovoltaic Devices. *Crit. Rev. Solid State Mater. Sci.* **2002**, *27*, 73–117.
44. Rogacheva, E. I. Nonstoichiometry in the I-III-VI_2 Compounds. *Inst. Phys. Conf. Ser., Sect. A* **1998**, *152*.
45. Merino, J. M.; Mahanty, S.; León, M.; Diaz, R.; Rueda, F.; Martin de Vidales, J. L. Structural Characterization of $CuIn_2Se_{3.5}$, $CuIn_3Se_5$, $CuIn_5Se_8$ Compounds. *Thin Solid Films* **2000**, *361−362*, 70–73.
46. Jayaraman, A.; Dernier, P. D.; Kasper, H. M.; Maines, R. G. Pressure-Induced Phase Transformations in Some I-III-VI_2 Semiconductors. *High Temp. − High Press.* **1977**, *9*, 97–102.
47. Norako, M. E.; Brutchey, R. L. Synthesis of Metastable Wurtzite $CuInSe_2$ Nanocrystals. *Chem. Mater.* **2010**, *22*, 1613–1615.
48. Zhang, S. B.; Wei, S.-H.; Zunger, A. Defect Physics of the $CuInSe_2$ Chalcopyrite Semiconductor. *Phys. Rev. B* **1998**, *57*, 9642–9656.
49. Leatherdale, C. A.; Kagan, C. R.; Morgan, N. Y.; Empedocles, S. A.; Kastner, M. A.; Bawendi, M. G. Photoconductivity in CdSe Quantum Dot Solids. *Phys. Rev. B* **2000**, *62*, 2669–2680.
50. Pallavicini, P.; Dacarro, G.; Galli, M.; Patrini, M. Spectroscopic Evaluation of Surface Functionalization Efficiency in the Preparation of Mercaptopropyltrimethoxysilane Self-Assembled Monolayers on Glass. *J. Colloid Interface Sci.* **2009**, *332*, 432–438.
51. Fafarman, A. T.; Koh, W.-k.; Diroll, B. T.; Kim, D. K.; Ko, D.-K.; Oh, S. J.; Ye, X.; Doan-Nguyen, V.; Crump, M. R.; Reifsnyder, D. C.; *et al.* Thiocyanate-Capped Nanocrystal Colloids: Vibrational Reporter of Surface Chemistry and Solution-Based Route to Enhanced Coupling in Nanocrystal Solids. *J. Am. Chem. Soc.* **2011**, *133*, 15753–15761.
52. Lu, W.; Liu, Q.; Sun, Z.; He, J.; Ezeolu, C.; Fang, J. Super Crystal Structures of Octahedral c-In_2O_3 Nanocrystals. *J. Am. Chem. Soc.* **2008**, *130*, 6983–6991.
53. Kang, Y.; Ye, X.; Chen, J.; Cai, Y.; Diaz, R. E.; Adzic, R. R.; Stach, E. A.; Murray, C. B. Design of Pt−Pd Binary Superlattices Exploiting Shape Effects and Synergistic Effects for Oxygen Reduction Reactions. *J. Am. Chem. Soc.* **2013**, *135*, 42–45.

54. Chen, J.; Ye, X.; Oh, S. J.; Kikkawa, J. M.; Kagan, C. R.; Murray, C. B. Bistable Magnetoresistance Switching in Exchange-Coupled $CoFe_2O_4$-Fe_3O_4 Binary Nanocrystal Superlattices by Self-Assembly and Thermal Annealing. *ACS Nano* **2013**, *7*, 1478–1486.
55. Ye, X.; Collins, J. E.; Kang, Y.; Chen, J.; Chen, D. T. N.; Yodh, A. G.; Murray, C. B. Morphologically Controlled Synthesis of Colloidal Upconversion Nanophosphors and Their Shape-Directed Self-Assembly. *Proc. Natl. Acad. Sci. U.S.A.* **2010**, *107*, 22430–22435.
56. Murray, C. B.; Kagan, C. R.; Bawendi, M. G. Synthesis and Characterization of Monodisperse Nanocrystals and Close-Packed Nanocrystal Assemblies. *Annu. Rev. Mater. Sci.* **2000**, *30*, 545–610.